Light Trapping in Single Elliptical Nanowires

Wenfu Liu [1,2,*], Yinling Wang [1], Xiaolei Guo [1], Jun Song [1], Xiao Wang [2] and Yasha Yi [2,3,*]

[1] School of Mechanical and Energy Engineering, Huanghuai University, Zhumadian, Henan 463000, China; wangyinling@huanghuai.edu.cn (Y.W.); guoxiaolei@huanghuai.edu.cn (X.G.); songjun@huanghuai.edu.cn (J.S.)

[2] Integrated Nano Optoelectronics Laboratory, University of Michigan, Dearborn, MI 48128, USA; xwa@umich.edu (X.W.)

[3] Energy Institute, University of Michigan, Ann Arbor, MI 48109, USA

* Correspondence:liuwenfu@huanghuai.edu.cn (W.L.); yashayi@umich.edu (Y.Y.)

Abstract: Light trapping in single nanowires (NWs) are of vital importance for photovoltaic applications. However, circular NWs (CNWs) can limit its light-trapping ability due to high geometrical symmetry. In this work, we present a detailed study of light trapping in single NWs with an elliptical cross-section (ENWs). We demonstrate that the ENWs exhibit significantly enhanced light trapping compared with the CNWs, which can be ascribed to the symmetry-broken structure that can orthogonalize the direction of light illumination and the leaky mode resonances (LMRs). That is, the elliptical cross-section can simultaneously increase the light path length by increasing the vertical axis and reshape the LMR modes by decreasing the horizontal axis. We found that the light absorption can be engineered via tuning the horizontal and vertical axes, the photocurrent is significantly enhanced by 374.0% (150.3%, 74.1%) or 146.1% (61.0%, 35.3%) in comparison with that of the CNWs with the same diameter as the horizontal axis of 100 (200, 400) nm or the vertical axis of 1000 nm, respectively. This work advances our understanding of how to improve light trapping based on the symmetry breaking from the CNWs to ENWs and provides a rational way for designing high-efficiency single or self-assembled NW photovoltaic devices.

Keywords: silicon; single nanowires; elliptical cross-section; absorption; photocurrent

1. Introduction

Single nanowire (NW) solar cells have increasingly attracted attention in recent years due to the following reasons [1-8]. Firstly, single NW solar cells can serve as nanoscale power sources integrated seamlessly with nanoelectronics. Secondly, Results from single NWs can subsequently provide feedback for the design of new functional NWs. Finally, single NWs can assemble to form NW arrays; results from single NWs can help understand the self-assembled NW-based solar cells [7-16]. It is well known that light trapping is an effective way to improve light absorption and enhance the photoelectric conversion efficiency of single NW solar cells. Moreover, the strong interaction between the incident light and a single NW has been applied to dramatically increase light absorption due to the leaky mode resonances (LMRs) [17-19]. However, the overall absorption performance of a single NW is still far below expectations owing to the narrow resonant peaks.

Therefore, a great variety of strategies have been employed to improve light trapping ability. It has been shown that the light absorption could be readily engineered by controlling the size, geometry and orientation of the NWs [20-26]. Our previous studies [27-29] showed that the light absorption could be further improved by introducing a non-absorbing dielectric shell (or graded dual shells) as the antireflection coating, which was experimentally and numerically demonstrated in the recent studies [30-34]. Recently, some new strategies have been implemented to improve the light-trapping capability of the NWs based on the symmetry breaking, including front-opening crescent design [35], rear-opening crescent design [36], off-axial core-shell design [37], asymmetrical nanovoid design [22] and partially capped design [38]. Comparing with the circular NWs (CNWs), elliptical

NWs (ENWs) provide the more possibility to tune light trapping, which has been applied to improve light trapping in single ellipsoids [39,40], NW arrays [41], nanocone arrays [42] and nanohole arrays [43,44]. However, to the best of our knowledge, very few investigations based on the symmetry breaking from the CNW to ENW have been explored to improve light trapping in single NWs so far.

In this work, we carry out detailed investigations on the light trapping effect of single ENWs. We demonstrate that the giant enhancement of the light absorption occurs when the ENWs replace the CNWs. The detailed analysis of the electric field, absorption mode profile and photogeneration rate shows that this enhancement is mainly attributed to the asymmetry breaking from the CNWs to ENWs. Specifically, the light path length can increase by increasing the vertical axis and the LMRs can reshape by decreasing the horizontal axis. Simulation results reveal that the photocurrent is significantly enhanced by 374.0% (150.3%, 74.1%) or 146.1% (61.0%, 35.3%) compared with that of the CNW with the same diameter as the horizontal axis of 100 (200, 400) nm or the vertical axis of 1000 nm, respectively.

2. Model and Methods

2.1. Model

Figure 1 schematically illustrates the cross-sectional views of a CNW and several ENWs. The horizontal and vertical axes of the ENWs are denoted by a and b. The horizontal (or vertical) axis is perpendicular (or parallel) to the light illumination direction, as shown using the colorful arrows in Figure 1. The values of a are chosen to be 400, 200 and 100 nm as the typical representative nanoscale size and the values of b are chosen to the range from 10 (oblate ENWs) to 1000 (prolate ENWs) nm. It should be noted that the CNWs are also shown for comparison, where the diameter D of the CNWs is chosen to be b to investigate the improved light trapping due to the reshaped LMRs by decreasing a, or a to investigate the improved light trapping owing to the increased light path length by increasing b. A wavelength-dependent refractive index of silicon is adopted from the experimental data [45].
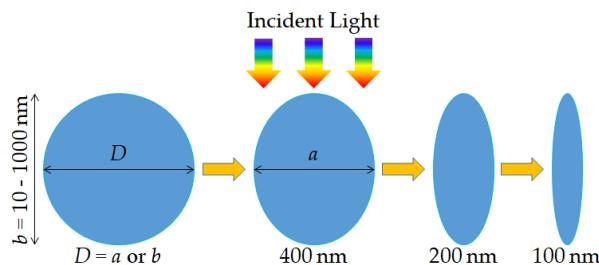
Figure 1. Schematics of the cross-section of a circle nanowire (CNW) and several elliptical nanowires (ENWs). The geometrical metrics used to describe the geometry of the ENWs, the horizontal axis a and the vertical axis b, are shown. Note here that three representative values of a are chosen to be 400, 200 and 100 nm, the range of b is from 10 to 1000 nm. The diameter D of the CNWs are chosen to be a or b for comparison, the material of the ENWs is set to be silicon as a representative semiconductor and the light illumination is perpendicular to the axis of the ENW from above.

2.2. Methods

Numerical simulations are carried out by solving Maxwell's equations based on two dimensional finite difference time domain (2D FDTD) method [46-48] by assuming that the length of the NWs are infinitely long compared to its cross-section, which can be referred to the work of Kim and co-workers for details [24-26,32]. In this simulation, the ENWs are illuminated perpendicularly by sunlight from the top, the wavelength range of the incident light is from 300 to 1100 nm with a step size of 5 nm considering solar radiation and the bandgap of silicon, the perfectly matched layers (PML) boundary conditions are applied to avoid any non-physical reflection with the boundaries, the total-field scattered-field (TFSF) method was adopted to ensure that a single NW interacts with an

infinite plane wave. Also, the minimum cell size of the FDTD mesh is set to from 0.05 to 5 nm corresponding to b (5 → 1000 nm) to guarantee the accuracy of the simulation results.

2.2.1. The Normalized Electric Field (E_r)

The normalized electric field (E_r) can be defined as [38]

$$E_r = E/E_0 \, , \tag{1}$$

where E is the electric field of the ENWs, which is obtained by FDTD numerical simulation, and E_0 is the electric field of the solar incident light, respectively.

2.2.2. The Absorption Mode Profile (P_{abs})

The wavelength-dependent absorption mode profile (P_{abs}) calculated from Poynting theorem, which can be expressed as [34,49-51]

$$P_{abs} = \frac{1}{2} \omega \varepsilon'' |E|^2 \, , \tag{2}$$

where ω is the angular frequency of the incident light and ε'' is the imaginary part of the permittivity of silicon, respectively.

2.2.3. The Absorption Efficiency (Q_{abs})

To qualify the light absorption performance of the ENWs, we define the absorption efficiency (Q_{abs}) as [34,49-51]:

$$Q_{abs} = C_{abs}/C_{geo} \, , \tag{3}$$

where C_{geo} is the projected area of the ENWs and C_{abs} is the absorption cross-section obtained by

$$C_{abs} = \frac{\int_V P_{abs} dV}{I_0} = k_0 \varepsilon_r'' \int_V |E_r|^2 \, dV \, , \tag{4}$$

where k_0 is the wave vector in air, ε_r'' is the imaginary part of the relative permittivity of silicon, V is the volume of the ENWs and I_0 is the solar incident light intensity expressed as [34,49-51]

$$I_0 = \frac{1}{2} c \varepsilon_0 |E_0|^2 \tag{5}$$

$$\varepsilon_r'' = \varepsilon''/\varepsilon_0 \, , \tag{6}$$

where c is the speed of light and ε_0 is the permittivity in air, respectively.

2.2.4. The Photogeneration Rate (G)

The spatially dependent photogeneration rate (G) is readily calculated by [52,53]

$$G = \int_{300}^{1100} \frac{P_{abs}}{\hbar \omega} d\lambda = \int_{300}^{1100} \frac{\varepsilon'' |E|^2}{2\hbar} d\lambda \, , \tag{7}$$

where $\hbar$ is the reduced Planck's constant and λ is the wavelength of the incident light. Note that when using Equation (7), each photon absorbed in ENW contributes to the photocurrent without considering recombination losses.

2.2.5. The Ultimate Photocurrent (J_{ph})

The overall light-trapping performance is evaluated using the ultimate photocurrent (J_{ph}) calculated by

$$J_{\mathrm{ph}} = \frac{q}{C_{geo}} \int_V GdV = q\int_{300}^{1100} \Gamma(\lambda)Q_{abs}(\lambda)d\lambda \, , \qquad (8)$$

where q is the elementary charge and Γ is the AM1.5G standard solar photon flux density spectrum. It should be noted here that 100% collection efficiency is assumed, which has been widely employed to evaluate the ultimate photocurrent [18,53].

2.2.6. The Photocurrent Enhancement Factor (PEF)

The photocurrent enhancement is evaluated by employing the photocurrent enhancement factor (PEF) using the relation:

$$\mathrm{PEF} = \left(J_{\mathrm{ph,ENWs}} - J_{\mathrm{ph,CNWs}}\right) \Big/ J_{\mathrm{ph,CNWs}} \, , \qquad (9)$$

where $J_{ph,ENWs}$ and $J_{ph,CNWs}$ are the photocurrent density for the ENWs and CNWs, respectively.

3. Results and Discussion

3.1. The Absorption Mechanism in single ENW

To understand the absorption mechanism responsible for the improved light-trapping ability of the ENW, we investigate the absorption efficiency (Q_{abs}), ultimate photocurrent (J_{ph}), normalized electric field (E_r), absorption mode profile (P_{abs}) and photogeneration rate (G), respectively. Note here that $a = 200$, $b = 500$ nm and $D = a = 200$ or $D = b = 500$ nm denotes the cases of the CNW with the same a or b for comparison, respectively.

3.1.1. The Absorption Efficiency (Q_{abs})

To quantitatively characterize the absorption enhancement of the ENW in comparison with the CNW, we first examine the absorption spectra obtained by Equation (3). In Figure 2, we show λ-dependent Q_{abs} spectra of the ENW with $a = 200$ and $b = 500$ nm and the CNW with $D = b = 500$ nm under normally-incident transverse-magnetic (TM), transverse-electric (TE) and unpolarized light, respectively. It is important to emphasize that the unpolarized illumination, like sunlight, is calculated by averaging TM and TE light illumination. TM and TE lights are shown in the inset in the top center of Figure 1a and Figure 1b, respectively. It is clear that the light absorption of the ENW is much bigger than that of the CNW in the short-wavelength range of $\lambda < \lambda_{cTM} \sim 675$, $\lambda < \lambda_{cTE} \sim 545$ or $\lambda < \lambda_c \sim 670$ nm for TM, TE or unpolarized light (except for several narrow peaks, for example, $\lambda = 555$ nm for unpolarized light), which can result in a significant photocurrent enhancement since the Q_{abs} spectra of the CNW well matches the solar spectrum according to Equation (8). In comparison, the light absorption of the ENW seems to be comparable in the long-wavelength range of $\lambda > \lambda_{cTM}$, $\lambda > \lambda_{cTE}$ or $\lambda > \lambda_c$, which can lead to a little contribution to the photocurrent enhancement. Note that λ_{cTM}, λ_{cTE} and λ_c are the characteristic wavelengths, below which the light absorption is always enhanced and can be readily determined for fixed a, b and D.

Moreover, the Q_{abs} spectra for TM light present some characteristics different from that for TE light. Specifically, compared to the Q_{abs} spectra of the CNW with $D = b = 500$ nm, the number of resonant peaks increases (5 → 7) in the wavelength range of $\lambda < \lambda_{cTM}$ due to the blue-shift of peaks and the light absorption slightly improve for TM light, for example, 0.62 → 0.73 for the fourth peak, however, the number of resonant peaks decreases (10 → 7) in the whole wavelength range and the light absorption dramatically enhance in the wavelength range of $\lambda < \lambda_{cTE}$ at the same time, for instance, 0.53 → 1.44 for the fourth peak. Note here that some Q_{abs} values for TE light exceed unity,

which is attributed to the fact that the absorption cross-section is greater than the physical cross-section. All in all, the absorption results indicate the great potential of the single ENW in improving light trapping due to the symmetry-broken structure from the CNW to ENW.
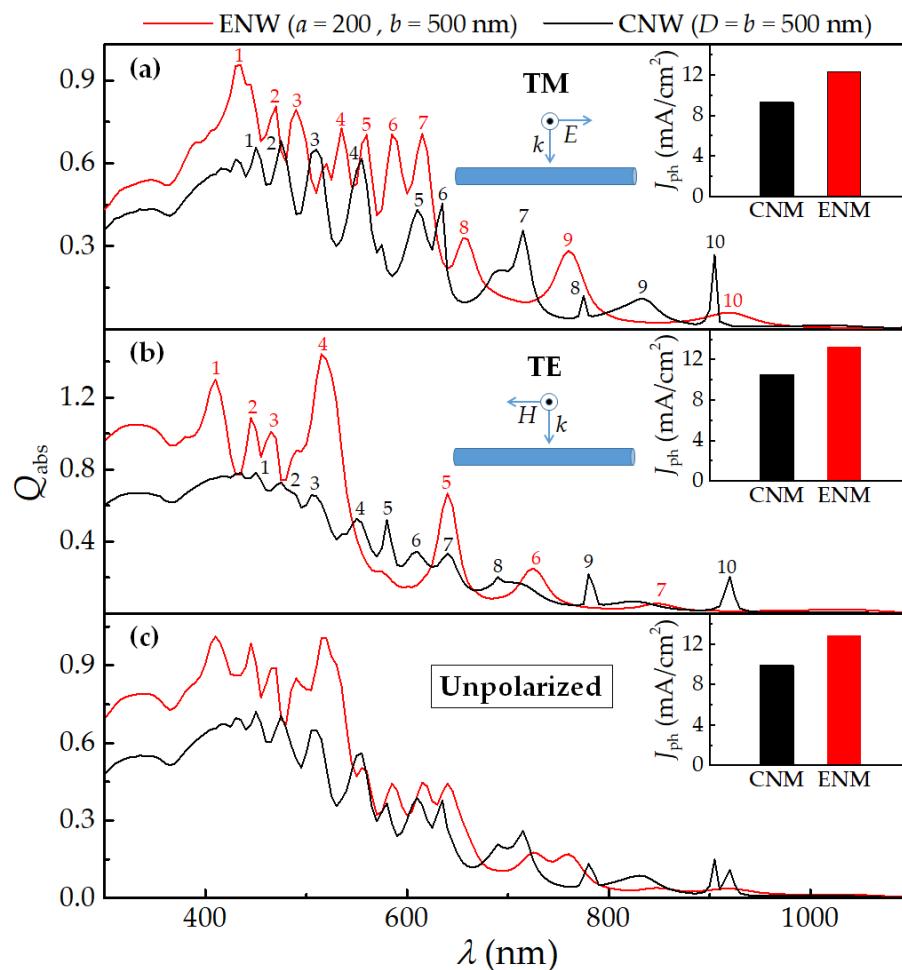
Figure 2. Absorption efficiency (Q_{abs}) of the CNW and ENW as a function of wavelength (λ) for (**a**) transverse-magnetic (TM), (**b**) transverse-electric (TE) and (**c**) unpolarized light illumination, respectively. The insets at the top center illustrate the illumination geometries for (**a**) TM (electric field parallel to the axis of the ENW) and (**b**) TE (electric field perpendicular to the axis of the ENW) light illumination, respectively. Also, the insets at the top right corner show the ultimate photocurrent (J_{ph}) of the CNW and ENW for (**a**) TM, (**b**) TE and (**c**) unpolarized light, respectively. Note that $a = 200$ and $D = b = 500$ nm

3.1.2. The Ultimate Photocurrent (J_{ph})

To evaluate the light-trapping performance of the ENW, we then calculated the ultimate photocurrent (J_{ph}) according to Equation (8). For a direct comparison, in the insets of the upper right corner of Figure 1, we show J_{ph} of the ENW and CNW corresponding to Q_{abs} for TM, TE and unpolarized light illumination, respectively. It is observed that J_{ph} of the ENW is much bigger than that of the CNW with $D = b = 500$ nm. J_{ph} for TM, TE and unpolarized light illumination reaches 12.32, 13.24 and 12.78 mA/cm², which is 32.5%, 26.6% and 29.4% higher than that of the CNW (9.30, 10.46 and 9.88 mA/cm²), respectively. It is worth noting that the photocurrent enhancement is mainly ascribed to the reshaped LMRs caused by decreasing a (that is $D \rightarrow a$, here 500 $\rightarrow$ 200 nm) compared to the CNW with $D = b = 500$ nm, as discussed later. Besides, J_{ph} can significantly enhance due to the increased light path length by increasing b ($D \rightarrow b$, here 200 $\rightarrow$ 500 nm) compared with the CNW with $D = a = 200$ nm. J_{ph} is 50.2%, 82.9% and 65.5% higher than that of the CNW (8.20, 7.24 and 7.72

mA/cm²) [29] for TM, TE and unpolarized light illumination, respectively. The photocurrent results further indicate the huge potential of light trapping in single ENW for photovoltaic applications.

3.1.3. The Normalized Electric Field (E_r)

To understand the mechanism of light trapping in single ENW, we first examine the normalized electric field (E_r) calculated by Equation (1) [38]. In Figure 3, we present the E_r profiles of the CNW ($D = b$ =500 nm) and the ENW (a = 200 and b = 500 nm) corresponding to the positions denoted by Araba numerals in Figure 2a,b under TM and TE light illumination, respectively. Note that Figure 3a,c show the E_r profiles of the CNW for TM (λ = 450, 475, 510, 550, 610, 635, 715, 775, 835 and 905 nm) and TE (λ = 450, 475, 505, 550, 580, 610, 640, 690, 780 and 920 nm) light illumniation, while Figure 3b,d show those of the ENW for TM (λ = 435, 470, 490, 535, 560, 585, 615, 655, 760 and 920 nm) and TE (λ = 410, 440, 465, 515, 640, 725 and 850 nm) light illumination, respectively.
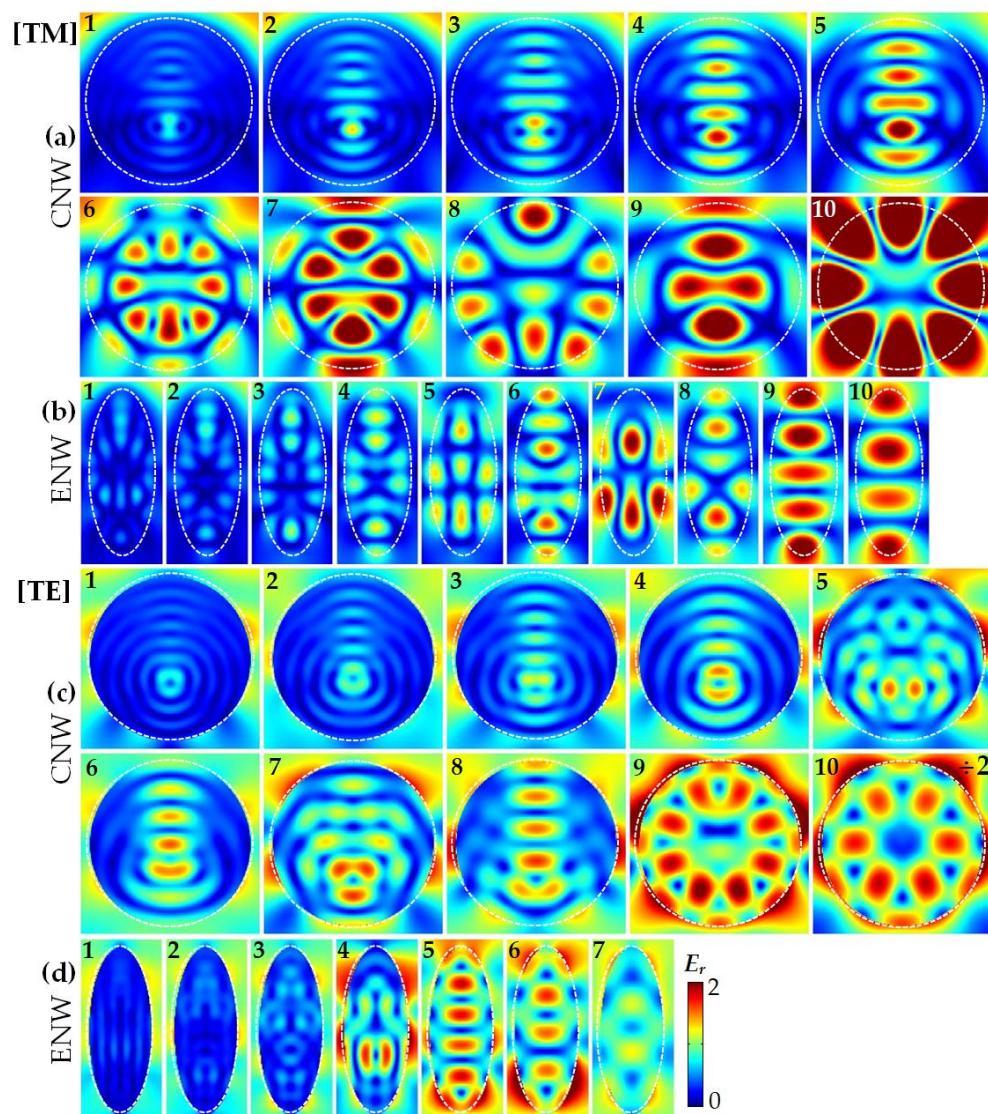
Figure 3. The representative normalized electric field (E_r) profiles of the CNW and ENW at the absorption peaks indicated by Araba numerals in Figure 2a,b: (**a**,**b**) for TM and (**c**,**d**) for TE light illumination (with an identical color scale); (**a**,**c**) for the CNW with $D = b$ = 500 nm and (**b**,**d**) for the ENW with a = 200 and b = 500 nm, respectively. Note that the E_r intensity in **c**(10) is properly shrunk for better illustration.

It is observed that there are common characteristics of the E_r profiles between the ENW and CNW. Firstly, the absorption enhancement of the ENW is attributed to the excitation of the LMRs,

likewise in CNW [17,18], which can confine light by multiple total internal reflections at the ENW/air interface when the wavelength of the incident light matches one of the LMRs supported by the ENW. The LMRs can be termed as TM_{ml} or TE_{ml}, where m and l describe the azimuthal mode number and the radial order of the resonances, respectively. For example, the E_r profiles of the ENW in Figure 3b(10) and Figure 3d(7) show more characteristics of the TM_{12} and TE_{11} modes of the CNW, respectively. Secondly, both NW configurations show much higher E_r intensities in the long- than short-wavelength range. Specifically, the E_r intensities for both NW configurations are much higher in Figure 3a,b(5-10) than Figure 3a,b(1-4) for TM light, while the E_r intensities of the CNW in Figure 3c(5-10) and the ENW in Figure 3d(4-7) are much bigger than those of the CNW in Figure 3c(1-4) and the ENW in Figure 3d(1-3) for TE light, respectively, which is attributed to the fact that ε_r'' is much smaller in the long- than short-wavelength range, resulting in a stronger resonance.

More importantly, there are many distinct characteristics of the E_r profiles for both NW configures due to the symmetry breaking from the CNW to ENW. Firstly, the E_r profiles of the CNW exhibit a large number of exact (for example, TM_{51} in Figure 3a(8) and TE_{13} in Figure 3c(9)) and approximate degeneracies (for example, TM_{51} in Figure 3a(10) and TE_{13} in Figure 3c(10)). In contrast, the E_r profiles of the ENW exhibit different numbers, positions and modes of the resonant peaks between TM and TE light, indicating the higher tunability of light trapping in ENW than CNW. Secondly, the E_r intensities at some resonant peaks are much larger only near the vertical axis of the CNW (for example, Figure 3a(1-5) for TM light and Figure 3c(1-4,6,8) for TE light), while those at all resonant peaks are much bigger inside the whole ENW owing to the excitation of more complex LMRs in the short-wavelength range (for example, Figure 3b(1-4) for TM light and Figure 3d(1-3) for TE light), indicating the more vital interaction of incident light with the ENW, leading to a more significant absorption enhancement comparison with the CNW.

3.1.4. The Absorption Mode Profile (P_{abs})

To further understand the physics behind light trapping in single ENW, we then examine the absorption mode profile (P_{abs}) calculated by Equation (2) [22,24,36,50,52]. In Figure 4, we present the normalized P_{abs} of the CNW ($D = b = 500$ nm) and the ENW ($a = 200$ and $b = 500$ nm) corresponding to the same positions denoted by Araba numerals in Figure 2 and Figure 3 under TM and TE light illumination, respectively. Note that Figure 4a,c show the normalized P_{abs} of the CNW for TM and TE light, while Figure 4b,d show those of the ENW, respectively. It is observed that both NW configurations exhibit much higher absorption in the short- and medium- than long-wavelength range. Specifically, the light absorption for both NW configurations is much higher in Figure 4a,b(1-7) than Figure 4a,b(8-10) for TM light, while the light absorption of the CNW in Figure 4c(1-7) and the ENW in Figure 4d(1-5) is much bigger than that of the CNW in Figure 4c(8-10) and the ENW in Figure 4d(6-7) for TE light, respectively, which is attributed to the fact that ε_r'' is much greater in the short- and medium- than long-wavelength range, leading to a stronger absorption in the short- and medium wavelength range.

It is worth noting that the match between ε_r'' and E_r becomes another essential factor in evaluating the absorption in the specific wavelength according to Equation (2). For instance, although the E_r intensities of the ENW at $\lambda = \lambda_{10} = 920$ nm for TM light is much larger, the corresponding ε_r'' is the smallest, which still leads to a lower absorption, while although those of the ENW at $\lambda = \lambda_1 = 410$ nm for TM light is the smallest, the corresponding ε_r'' is much larger, which results in a more significant absorption. It is readily observed that the spatially localized absorption sites of the ENW in both ends of the horizontal axis are considerably increased compared to the CNW, and more absorption sites appear and fill in the whole ENW. Such enhanced strong light-matter interaction results in a giant absorption enhancement, as shown in Figure 2.
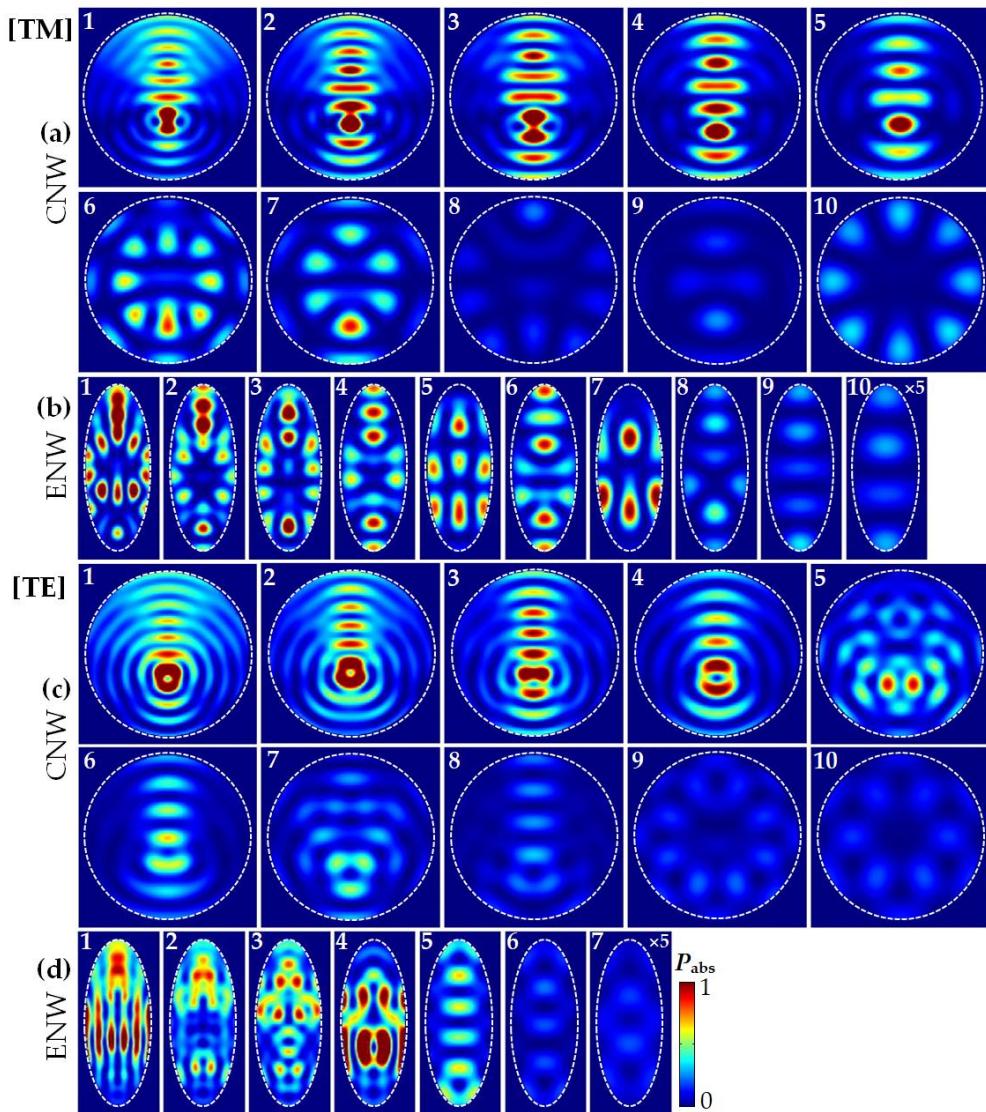
Figure 4. The representative normalized absorption mode profiles (P_{abs}) for the CNW and ENW at the absorption peaks indicated by Araba numerals in Figure 2a,b and Figure 3: **(a,b)** for TM and **(c,d)** for TE light illumination (with an identical color scale); **(a,c)** for the CNW with $D = b = 500$ nm and **(b,d)** for the ENW with $a = 200$ and $b = 500$ nm, respectively. Note that P_{abs} in **b**(10) and **d**(7) are properly magnified for better illustration.

3.1.5. The Photogeneration Rate (G)

To further confirm the physical mechanism discussed above, we show the photogeneration rate (G) calculated Equation (6). In Figure 5, we present the normalized G profiles of the CNW ($D = b = 500$ nm) and the ENW ($a = 200$ and $b = 500$ nm) for TM and TE light illumination. Note that Figure 5a,c show the normalized G profiles of the CNW for TM and TE light, while Figure 5b,d show those of the ENW, respectively. It is observed in Figure 5a,b that the absorption of the ENW is much stronger at both ends of the horizontal axis than that of the CNW for TM light. At the same time, it is observed in Figure 4c,d that the absorption of the ENW fills in the whole NW for TE light, consistent with the results discussed above. These results further demonstrate that this enhancement arises mainly from the excitation of more LMR modes caused by decreasing a compared to the CNW with $D = b$. In other words, the ENW can better interact with the incident light compared to the CNW, leading to more resonant absorption sites appear and fill in the whole ENW.
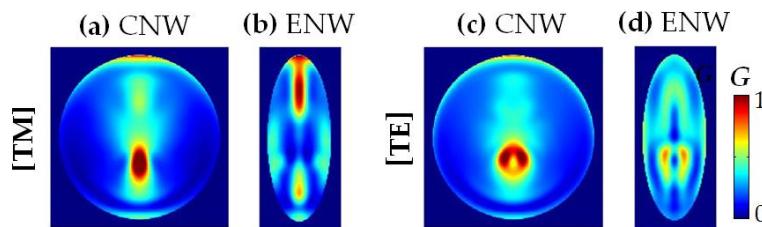
Figure 5. The normalized photogeneration rate (G) profiles for the CNW and ENW: (**a**,**b**) for TM and (**c**,**d**) for TE light illumination (with an identical color scale); (**a**,**c**) for the CNW with $D = b = 500$ nm and (**b**,**d**) for the ENW with $a = 200$ and $b = 500$ nm, respectively.

3.2. The Light Trapping Performance of Single ENWs

To verify that the high absorption enhancement is not just specific for the dimension discussed above, we calculate Q_{abs} and J_{ph} of the ENWs with $b = 10 \rightarrow 1000$ nm and $a = 400, 200$ and 100 nm, Q_{abs} and J_{ph} of the CNWs with $D = b$ are investigated for comparison.

3.2.1. The Absorption Efficiency of Single ENWs

To evaluate the light-trapping performance of the ENWs for photovoltaic applications, we first investigate the effect of its geometrical parameters on the absorption efficiency calculated using Equation (3). In Figure 6, we show 2D contour maps of λ-dependent Q_{abs} as a function of b ($10 \rightarrow 1000$ nm) for the ENWs with $a = 400, 200$ and 100 nm for TM and TE light illumination, respectively. Note that the Q_{abs} spectra of the CNWs with $D = b$ is also shown for comparison. It is observed that the Q_{abs} spectra of the ENWs show the extensive wavelength tenability, and the light absorption of the NEWs with $b > a$ is dramatically enhanced compared to that of the CNWs for both polarized lights.

On the one hand, the Q_{abs} spectra of the ENWs exhibit some characteristics similar to the CNWs. Firstly, the number of resonant peaks increases. For example, Figure 6d shows five and eleven peaks for the ENWs with $b = 300$ and 900 nm, respectively. Secondly, the peaks tend to red-shift with increasing b. For instance, in Figure 6d, the peak at near $\lambda = 420$ nm for the ENW with $b = 300$ nm can shift substantially to about $\lambda = 800$ nm for the ENW with $b = 1000$ nm. Finally, the resonant peaks in different ENWs may originate from entirely different resonances. For example, Figure 6d shows the peaks near $\lambda = 600$ nm for the ENWs with $b = 300$ and 600 nm.

On the other hand, the Q_{abs} spectra of the ENWs also show some characteristics different from the CNWs. Firstly, the light absorption of the CNWs is gradually weakened due to the weak LMRs with increasing D. In contrast, the light absorption of the ENWs is significantly enhanced with increasing b for various a for both polarized lights, which can be attributed to the reshaped LMRs due to the small size of the horizontal axis. Secondly, the Q_{abs} spectra of the ENWs with large $a = 400$ and 200 nm show some enhanced absorption sites owing to the superposition of resonant peaks, which may result from different LMR modes caused by the size difference of the horizontal and vertical axes. These enhanced absorption sites are greatly strengthened and tend to blue-shift with decreasing $a = 400 \rightarrow 200$ nm, and then the resonant peaks for TM light exhibit similar peaks with the CNWs, while those for TE light present some new peaks utterly different from the CNWs with further deceasing $a = 200 \rightarrow 100$ nm. For example, the number of resonant peaks decreases, and the peaks tend to blue-shift, but the light absorption is dramatically enhanced. Thirdly, with decreasing $a = 400 \rightarrow 100$ nm, the light absorption is significantly enhanced in the short-wavelength range of $\lambda < \sim 420$ nm. Finally, The light absorption for TE light is much higher than that for TM light, resulting in a bigger photocurrent for TE light.

It is worth noting here that the light absorption near $\lambda = 350$ nm of the CNWs with small D (< 100 nm) is higher than that of the ENWs for TM light due to the excitation of the strongest TM_{01} and second strongest TM_{11}/TE_{01} modes [18,28]; however, such small NWs are not practical for photovoltaic applications. In a word, these Q_{abs} spectra indicate that the light absorption of the ENWs with $b > a$ can be significantly enhanced compared to that of the CNWs.
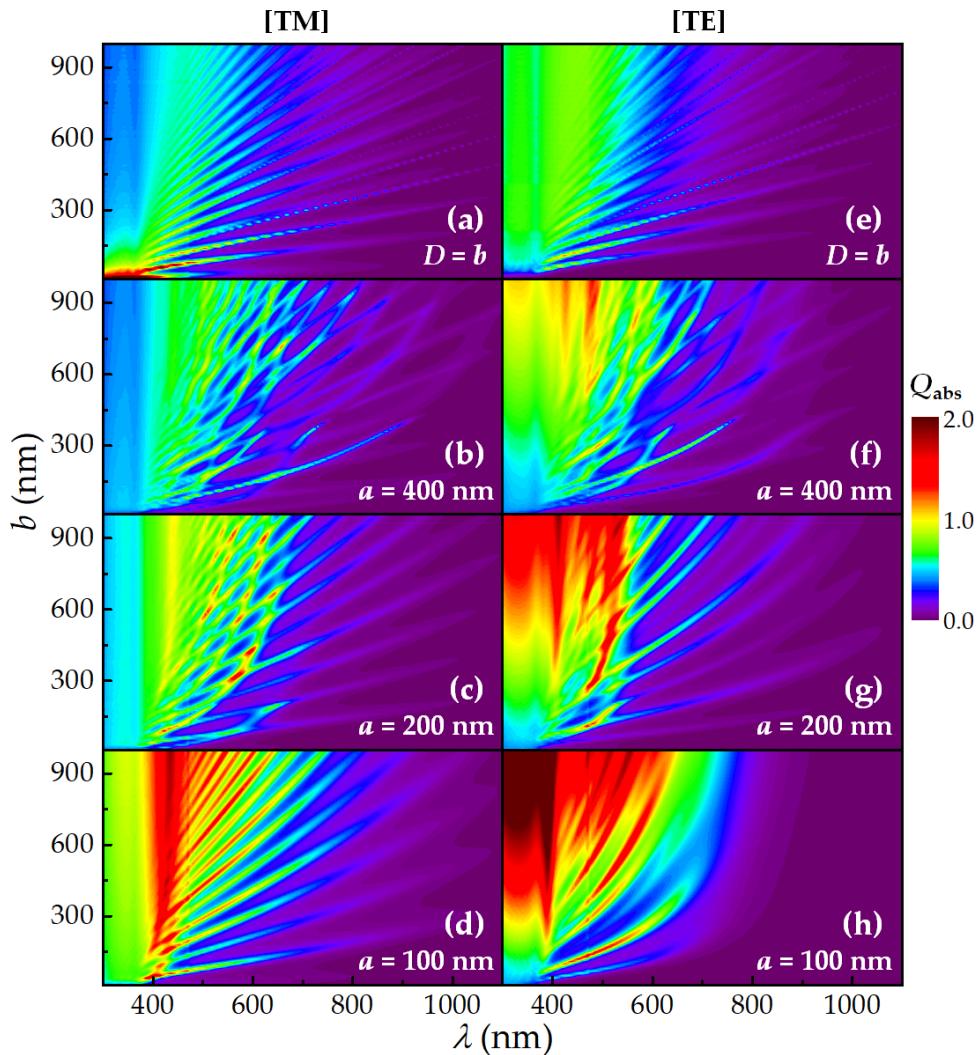
Figure 6. Q_{abs} versus b and λ for the CNWs and ENWs: (**a,b,c,d**) for TM and (**e,f,g,h**) for TE light illumination (with an identical color scale); (**a,e**) for the CNW with $D = b$; (**b,f;c,g; d,h**) for the ENWs with a = 400, 200 and 100 nm, respectively.

3.2.2. The ultimate photocurrent of Single ENWs

To evaluate the light-trapping performance of the ENWs for photovoltaic applications, we now investigate the influence of geometrical parameters on the ultimate photocurrent (J_{ph}) calculated using Equation (8). In Figure 7a-c, we show J_{ph} as a function of b (10 $\rightarrow$ 1000 nm) of the ENWs with a = 400, 200 and 100 nm and the CNWs with $D = b$ for TM, TE and unpolarized light illumination, respectively. It is shown that for $b < a$, with increasing b, J_{ph} of the ENWs with small b (< 100 nm) is much smaller than that of the CNWs due to the excitation of the strongest TM_{01} and second strongest TM_{11}/TE_{01} modes of the CNWs [18,28] and then can be slightly enhanced when $b \rightarrow a$ due to the superposition of resonant peaks, this enhancement is more evident for large than small a. More importantly, for $b > a$ (except for $a \rightarrow b$), with increasing b, J_{ph} of the ENWs is dramatically enhanced compared to the CNWs. Specifically, J_{ph} periodically increases for large a = 400 $\rightarrow$ 200 nm and linearly increases for small a = 100 nm.

In the insets of Figure 7, we show the normalized G profiles of a CNW and three ENWs for TM and TE light illumination, respectively. Note here that $D = b$ = 1000 nm, and a = 400, 200 and 100 nm, respectively. As presented above, the absorption enhancement of the ENWs only occurs near the vertical axis, leading to the small photocurrent enhancement with increasing b. However, with the symmetry breaking from CNWs to ENWs (a = 1000 $\rightarrow$ 400 $\rightarrow$ 200 $\rightarrow$ 100 nm), the LMR modes are

reshaped due to the size decrease of the horizontal axis, and the absorption enhancement sites better fill in the whole ENWs for both TM and TE lights, especially TE light.

Finally, we show in Figure 5c the photocurrent enhancement factors (PEFs) defined by Equation (9). It is readily observed that J_{ph} of the ENWs with $b > a$ (except $a \rightarrow b$) is much larger than the CNWs. In particular, J_{ph} reaches 29.53, 19.32 and 16.23 mA/cm² for a = 100, 200 and 400 nm, which is 146.1%, 61.0% and 35.3% much larger than that of the CNW with $D = b$ = 1800 nm (12.00 mA/cm²) due to the reshaped LMRs caused by the small size of the horizontal axis and 374.0%, 150.3% and 74.1% much larger than that of the CNW with $D = a$ = 100 (6.23 mA/cm²), 200 (7.72 mA/cm²) and 400 (9.32 mA/cm²) due to the increased light path length by the vertical axis, respectively.
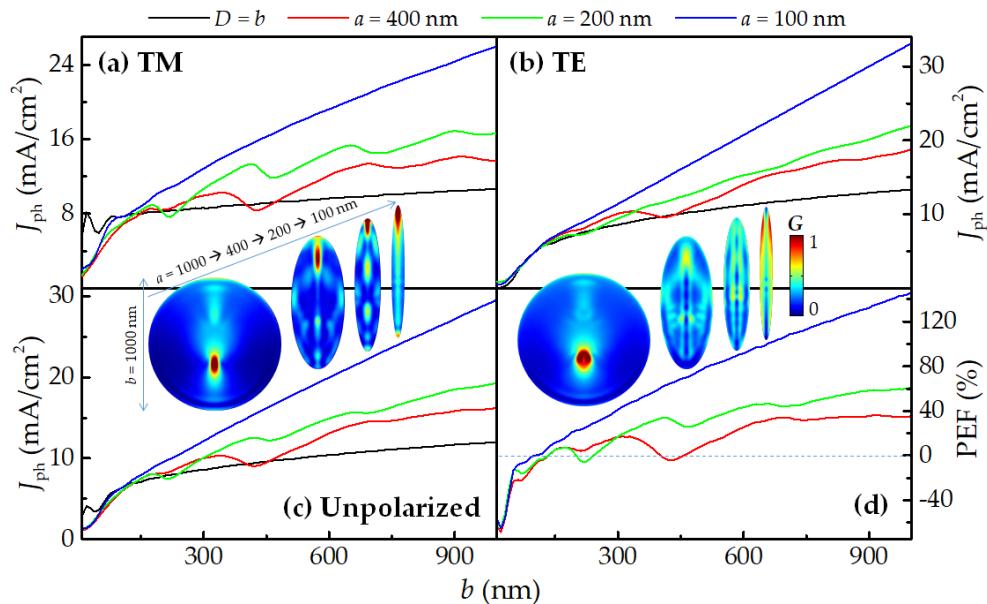
Figure 7. J_{ph} versus b of the CNWs with $D = b$ and the ENWs with a = 400, 200 and 100 nm for (**a**) TM, (**b**) TE and (**c**) unpolarized light illumination, respectively. (**d**) the photocurrent enhancement factor (PEF) versus b of the ENWs compared to the CNWs. The insets illustrate the normalized G profiles of the CNWs with $D = b$ = 1000 nm and the ENWs with b = 1000 nm and a = 400, 200 and 100 nm for TM and TE light illumination (with an identical color scale), respectively.

4. Conclusions

In summary, we demonstrated the enhanced light trapping from the CNW to ENW. The influences of the geometrical parameters of the ENW on the light trapping performance are numerically investigated. It is found that the elliptical cross-section can lead to significantly improved light trapping. The examination of the spatial profiles of the electric field, absorption mode and photogeneration rate reveals that the enhancement effect results from the symmetry-broken structure, which can simultaneously realize the increase of the light path length by the vertical axis and the reshaped LMRs by the horizontal axis. The simulation results show that the photocurrent is significantly enhanced by 374.0% (150.3%, 74.1%) or 146.1% (61.0%, 35.3%) in comparison with that of the CNW with the same diameter as the horizontal axis of 100 (200, 400) nm or the vertical axis of 1000 nm, respectively. Therefore, such an elliptical nanowire can be applied to various semiconductors to improve light trapping and provides a promising approach for the future development of high-efficiency single or self-assembled NW solar cells.

Author Contributions: Conceptualization, W.L. and Y.Y.; methodology, W.L. and Y.W.; software, W.L. and X.W; investigation, W.L. and X.G.; writing—original draft preparation, W.L and J.S.; writing—review and editing, W.L. and Y.Y. All authors have read and agreed to the published version of the manuscript.

Funding: This research was funded by the National Natural Science Foundation of China (Grant No. 61404057, 51801068 and 11875284), Key disciplines Fund for Optical Engineering in Henan Province (Grant No. 2018119) and Key Youth Teacher of Universities in Henan Province (Grant No. 2016GGJS-145).

Acknowledgments: We would like to thank the China Scholarship Council (Grant No. 201902720047) and the Master's Program on Energy and Power Engineering at Huanghuai University.

Conflicts of Interest: The authors declare no conflict of interest.

References

1. Tian, B.; Zheng, X.; Kempa, T.J.; Fang, Y.; Yu, N.; Yu, G.; Huang, J.; Lieber, C.M. Coaxial silicon nanowires as solar cells and nanoelectronic power sources. *Nature* **2007**, *449*, 885-889, doi:10.1038/nature06181.
2. Nehra, M.; Dilbaghi, N.; Marrazza, G.; Kaushik, A.; Abolhassani, R.; Mishra, Y.K.; Kim, K.H.; Kumar, S. 1D semiconductor nanowires for energy conversion, harvesting and storage applications. *Nano Energy* **2020**, *76*, 104991, doi:10.1016/j.nanoen.2020.104991.
3. Li, Z.; Tan, H.H.; Jagadish, C.; Fu, L. III–V Semiconductor Single Nanowire Solar Cells: A Review. *Adv. Mater. Technol.* **2018**, *3*, 1800005, doi:10.1002/admt.201800005.
4. Kempa, T.J.; Day, R.W.; Kim, S.-K.; Park, H.-G.; Lieber, C.M. Semiconductor nanowires: a platform for exploring limits and concepts for nano-enabled solar cells. *Energy Environ. Sci.* **2013**, *6*, 719-733, doi:10.1039/C3EE24182C.
5. Christesen, J.D.; Zhang, X.; Pinion, C.W.; Celano, T.A.; Flynn, C.J.; Cahoon, J.F. Design principles for photovoltaic devices based on Si nanowires with axial or radial p–n junctions. *Nano Lett.* **2012**, *12*, 6024-6029, doi:10.1021/nl303610m.
6. Zhan, Y.; Li, X.; Li, Y. Numerical Simulation of Light-Trapping and Photoelectric Conversion in Single Nanowire Silicon Solar Cells. *IEEE J. Sel. Top. Quantum Electron.* **2013**, *19*, 1-8, doi:10.1109/jstqe.2013.2246771.
7. Tian, B.; Kempa, T.J.; Lieber, C.M. Single nanowire photovoltaics. *Chem. Soc. Rev.* **2009**, *38*, 16-24, doi:10.1039/B718703N.
8. Tang, J.; Huo, Z.; Brittman, S.; Gao, H.; Yang, P. Solution-processed core-shell nanowires for efficient photovoltaic cells. *Nat. Nanotechnol.* **2011**, *6*, 568-572, doi:10.1038/NNANO.2011.139.
9. Holm, J.V.; Jørgensen, H.I.; Krogstrup, P.; Nygård, J.; Liu, H.; Aagesen, M. Surface-passivated GaAsP single-nanowire solar cells exceeding 10% efficiency grown on silicon. *Nat. Commun.* **2013**, *4*, 1498, doi:10.1038/ncomms2510.
10. Yuan, X.; Chen, X.; Yan, X.; Wei, W.; Zhang, Y.; Zhang, X. Absorption-Enhanced Ultra-Thin Solar Cells Based on Horizontally Aligned p–i–n Nanowire Arrays. *Nanomaterials* **2020**, *10*, 1111, doi:10.3390/nano10061111.
11. Chen, W.; Roca i Cabarrocas, P. Rational design of nanowire solar cells: from single nanowire to nanowire arrays. *Nanotechnology* **2019**, *30*, 194002, doi:10.1088/1361-6528/aaff8d.
12. Otnes, G.; Barrigón, E.; Sundvall, C.; Svensson, K.E.; Heurlin, M.; Siefer, G.; Samuelson, L.; Åberg, I.; Borgström, M.T. Understanding InP Nanowire Array Solar Cell Performance by Nanoprobe-Enabled Single Nanowire Measurements. *Nano Lett.* **2018**, *18*, 3038-3046, doi:10.1021/acs.nanolett.8b00494.
13. Song, K.-D.; Kempa, T.J.; Park, H.-G.; Kim, S.-K. Laterally assembled nanowires for ultrathin broadband solar absorbers. *Opt. Express* **2014**, *22*, A992-A1000, doi:10.1364/OE.22.00A992.
14. Zhang, X.; Pinion, C.W.; Christesen, J.D.; Flynn, C.J.; Celano, T.A.; Cahoon, J.F. Horizontal Silicon Nanowires With Radial p-n Junctions: A Platform for Unconventional Solar Cells. *J. Phys. Chem. Lett.* **2013**, *4*, 2002–2009, doi:10.1021/jz400533.
15. Floris, F.; Fornasari, L.; Bellani, V.; Marini, A.; Banfi, F.; Marabelli, F.; Beltram, F.; Ercolani, D.; Battiato, S.; Sorba, L., et al. Strong Modulations of Optical Reflectance in Tapered Core–Shell Nanowires. *Materials* **2019**, *12*, 3572, doi:10.3390/ma12213572.
16. Floris, F.; Fornasari, L.; Marini, A.; Bellani, V.; Banfi, F.; Roddaro, S.; Ercolani, D.; Rocci, M.; Beltram, F.; Cecchini, M. Self-Assembled InAs Nanowires as Optical Reflectors. *Nanomaterials* **2017**, *7*, 400, doi:10.3390/nano7110400.
17. Cao, L.; White, J.S.; Park, J.-S.; Schuller, J.A.; Clemens, B.M.; Brongersma, M.L. Engineering light absorption in semiconductor nanowire devices. *Nat. Mater.* **2009**, *8*, 643-647, doi:10.1038/nmat2477.
18. Cao, L.; Fan, P.; Vasudev, A.P.; White, J.S.; Yu, Z.; Cai, W.; Schuller, J.A.; Fan, S.; Brongersma, M.L. Semiconductor Nanowire Optical Antenna Solar Absorbers. *Nano Lett.* **2010**, *10*, 439-445, doi:10.1021/nl9036627.
19. Brönstrup, G.; Jahr, N.; Leiterer, C.; Csáki, A.; Fritzsche, W.; Christiansen, S. Optical properties of individual silicon nanowires for photonic devices. *ACS Nano* **2010**, *4*, 7113-7122, doi:10.1021/nn101076t.
20. Kim, S.; Cahoon, J.F. Geometric Nanophotonics: Light Management in Single Nanowires through Morphology. *Acc. Chem. Res.* **2019**, *52*, 3511-3520, doi:10.1021/acs.accounts.9b00515.
21. Choi, J.S.; Kim, K.-H.; No, Y.-S. Spatially localized wavelength-selective absorption in morphology-modulated semiconductor nanowires. *Opt. Express* **2017**, *25*, 22750-22759, doi:10.1364/OE.25.022750.

22. Zhang, C.; Yang, Z.; Wu, K.; Li, X. Design of asymmetric nanovoid resonator for silicon-based single-nanowire solar absorbers. *Nano Energy* **2016**, *27*, 611-618, doi:10.1016/j.nanoen.2016.08.017.

23. Luo, S.; Yu, W.B.; He, Y.; Ouyang, G. Size-dependent optical absorption modulation of Si/Ge and Ge/Si core/shell nanowires with different cross-sectional geometries. *Nanotechnology* **2015**, *26*, 085702, doi:10.1088/0957-4484/26/8/085702.

24. Kim, S.-K.; Song, K.-D.; Kempa, T.J.; Day, R.W.; Lieber, C.M.; Park, H.-G. Design of Nanowire Optical Cavities as Efficient Photon Absorbers. *ACS Nano* **2014**, *8*, 3707–3714, doi:10.1021/nn5003776.

25. Kim, S.-K.; Day, R.W.; Cahoon, J.F.; Kempa, T.J.; Song, K.-D.; Park, H.-G.; Lieber, C.M. Tuning Light Absorption in Core/Shell Silicon Nanowire Photovoltaic Devices through Morphological Design. *Nano Lett.* **2012**, *12*, 4971-4976, doi:10.1021/nl302578z.

26. Kempa, T.J.; Cahoon, J.F.; Kim, S.-K.; Day, R.W.; Bell, D.C.; Park, H.-G.; Lieber, C.M. Coaxial multishell nanowires with high-quality electronic interfaces and tunable optical cavities for ultrathin photovoltaics. *P. Natl. Acad. Sci. USA* **2012**, *109*, 1407-1412, doi:10.1073/pnas.1120415109.

27. Liu, W.; Oh, J.I.; Shen, W.Z. Light Trapping in Single Coaxial Nanowires for Photovoltaic Applications. *IEEE Electron Device Lett.* **2011**, *32*, 45-47, doi:10.1109/LED.2010.2086428.

28. Liu, W.; Oh, J.I.; Shen, W.Z. Light absorption mechanism in single c-Si (core)/a-Si (shell) coaxial nanowires. *Nanotechnology* **2011**, *22*, 125705, doi:10.1088/0957-4484/22/12/125705.

29. Liu, W.; Guo, X.; Xing, S.; Yao, H.; Wang, Y.; Bai, L.; Wang, Q.; Zhang, L.; Wu, D.; Zhang, Y., et al. Off-Resonant Absorption Enhancement in Single Nanowires via Graded Dual-Shell Design. *Nanomaterials* **2020**, *10*, 1740, doi:10.3390/nano10091740.

30. Zhong, Z.; Li, Z.; Gao, Q.; Li, Z.; Peng, K.; Li, L.; Mokkapati, S.; Vora, K.; Wu, J.; Zhang, G., et al. Efficiency enhancement of axial junction InP single nanowire solar cells by dielectric coating. *Nano Energy* **2016**, *28*, 106-114, doi:10.1016/j.nanoen.2016.08.032.

31. Solanki, A.; Gentile, P.; Boutami, S.; Calvo, V.; Pauc, N. Dielectric Coating-Induced Absorption Enhancement in Si Nanowire Junctions. *Adv. Opt. Mater.* **2015**, *3*, 120-128, doi:10.1002/adom.201400334.

32. Kim, S.-K.; Zhang, X.; Hill, D.J.; Song, K.-D.; Park, J.-S.; Park, H.-G.; Cahoon, J.F. Doubling Absorption in Nanowire Solar Cells with Dielectric Shell Optical Antennas. *Nano Lett.* **2015**, *15*, 753-758, doi:10.1021/nl504462e.

33. Yu, Y.; Ferry, V.E.; Alivisatos, A.P.; Cao, L. Dielectric Core–Shell Optical Antennas for Strong Solar Absorption Enhancement. *Nano Lett.* **2012**, *12*, 3674-3681, doi:10.1021/nl301435.

34. Li, X.; Zhan, Y.; Wang, C. Broadband enhancement of coaxial heterogeneous gallium arsenide single-nanowire solar cells. *Prog. Photovolt. Res. Appl.* **2015**, *23*, 628-636, doi:10.1002/pip.2480.

35. Yang, Z.; Cao, G.; Shang, A.; Lei, D.Y.; Zhang, C.; Gao, P.; Ye, J.; Li, X. Enhanced Photoelectrical Response of Hydrogenated Amorphous Silicon Single-Nanowire Solar Cells by Front-Opening Crescent Design. *Nanoscale Res. Lett.* **2016**, *11*, 233, doi:10.1186/s11671-016-1447-0.

36. Yang, Z.; Li, X.; Lei, D.Y.; Shang, A.; Wu, S. Omnidirectional absorption enhancement of symmetry-broken crescent-deformed single-nanowire photovoltaic cells. *Nano Energy* **2015**, *13*, 9-17, doi:10.1016/j.nanoen.2015.02.007.

37. Zhang, C.; Yang, Z.; Shang, A.; Wu, S.; Zhan, Y.; Li, X. Improved optical absorption of silicon single-nanowire solar cells by off-axial core/shell design. *Nano Energy* **2015**, *17*, 233-240, doi:10.1016/j.nanoen.2015.08.017.

38. Zhou, J.; Zhang, Z.; Wu, Y.; Xia, Z.; Qin, X. Significantly enhanced coupling to half-space irradiation using a partially capped nanowire for solar cells. *Nano Energy* **2018**, *45*, 61-67, doi:10.1016/j.nanoen.2017.12.027.

39. Sychugov, I.; Sangghaleh, F.; Bruhn, B.; Pevere, F.; Luo, J.W.; Zunger, A.; Linnros, J. Strong Absorption Enhancement in Si Nanorods. *Nano Lett.* **2016**, *16*.

40. Kolezas, G.D.; Zouros, G.P.; Pagiatakis, G.K.; Roumeliotis, J.A. All–Anisotropic Spheroidal Photonic Antennas: Theory and Modeling. *IEEE J. Sel. Top. Quantum Electron.* **2021**, *27*, 8300312, doi:10.1109/JSTQE.2020.3001650.

41. Wu, Y.; Xia, Z.; Liang, Z.; Zhou, J.; Jiao, H.; Cao, H.; Qin, X. Broadband absorption enhancement in elliptical silicon nanowire arrays for photovoltaic applications. *Opt. Express* **2014**, *22*, A1292-A1302, doi:10.1364/OE.22.0A1292.

42. Qin, X.; Xia, Z.; Wu, Y.; Zhou, J.; Zhang, Z. Enhanced light absorption in perpendicular elliptical silicon nanocone array for solar cells. *Appl. Opt.* **2017**, *56*, 2307-2313, doi:10.1364/AO.56.002307.

43. Xia, Z.; Qin, X.; Wu, Y.; Pan, Y.; Zhou, J.; Zhang, Z. Efficient broadband light absorption in elliptical nanohole arrays for photovoltaic application. *Opt. Lett.* **2015**, *40*, 5814-5817, doi:10.1364/OL.40.005814.

44. Qin, X.; Wu, Y.; Zhang, Z.; Xia, Z.; Zhou, J.; Zhu, J. Broadband light absorption enhancement in randomly rotated elliptical nanohole arrays for photovoltaic application. *Appl. Opt.* **2019**, *58*, 1152-1157.

45. Palik, E.D. *Handbook of Optical Constants of Solids*; Academic Press: London, UK, 1985; Vol. 1, pp. 547-552.

46. Kane, Y. Numerical Solution of Initial Boundary Value Problems Involving Maxwell's Equations in Isotropic Media. *IEEE Trans. Antennas Propag.* **1966**, *14*, 302-307, doi:10.1109/TAP.1966.1138693.

47. Taflove, A.; Hagness, S.C. *Computational Electrodynamics: The Finite-Difference Time-Domain Method*, 3rd ed.; Artech House: Norwood, MA, USA, 2005.

48. Ee, H.S.; Song, K.D.; Kim, S.K.; Park, H.G. Finite-Difference Time-Domain Algorithm for Quantifying Light Absorption in Silicon Nanowires. *Isr. J. Chem.* **2012**, *52*, 1027-1036, doi:10.1002/ijch.201200061.

49. Bohren, C.F.; Huffman, D.R. *Absorption and Scattering of Light by Small Particles* John Wiley & Sons, Inc.: New York, USA, 1998; pp. 57-81, 202-204.

50. Zhou, L.; Yu, X.; Zhu, J. Metal-Core/Semiconductor-Shell Nanocones for Broadband Solar Absorption Enhancement. *Nano Lett.* **2014**, *14*, 1093-1098, doi:10.1021/nl500008y.

51. Mann, S.A.; Garnett, E.C. Extreme Light Absorption in Thin Semiconductor Films Wrapped around Metal Nanowires. *Nano Lett.* **2013**, *13*, 3173-3178, doi:10.1021/nl401179h.

52. Ferry, V.E.; Polman, A.; Atwater, H.A. Modeling light trapping in nanostructured solar cells. *ACS Nano* **2011**, *5*, 10055-10064, doi:10.1021/nn203906t.

53. Munday, J.N.; Atwater, H.A. Large integrated absorption enhancement in plasmonic solar cells by combining metallic gratings and antireflection coatings. *Nano Lett.* **2010**, *11*, 2195-2201, doi:10.1021/nl101875t.